JGR Atmospheres

RESEARCH ARTICLE
10.1029/2020JD033425

Special Section:
Atmospheric Rivers: Intersection of Weather and Climate

Examination of Global Midlatitude Atmospheric River Lifecycles Using an Object-Oriented Methodology

Eric J. Shearer[1], Phu Nguyen[1], Scott L. Sellars[2], Bita Analui[1], Brian Kawzenuk[3], Kuo-lin Hsu[1], and Soroosh Sorooshian[1,4]

[1]Center for Hydrometeorology and Remote Sensing (CHRS), Department of Civil and Environmental Engineering, Henry Samueli School of Engineering, University of California, Irvine, Irvine, CA, USA, [2]Qualcomm Institute, California Institute of Telecommunications and Information Technology (Calit2), University of California, San Diego, San Diego, CA, USA, [3]Center for Western Weather and Water Extremes (CW3E), Scripps Institute of Oceanography, University of California, San Diego, San Diego, CA, USA, [4]Department of Earth Systems Science, University of California, Irvine, Irvine, CA, USA

Abstract Tracking atmospheric rivers (ARs) across their lifecycles is a field of recent interest with a multitude of emerging methodologies. The CONNected-objECT (CONNECT) algorithm is adapted for the tracking of global midlatitude AR lifecycles and associated precipitation by implementing a seeded region growing segmentation algorithm, creating the AR-CONNECT algorithm. To facilitate the permissiveness of the methodology, AR-CONNECT is without hard-coded geometric criteria yet is still shown to extract synoptic-scale elongated objects >99.99% of the time. One of the consequences of the methodology is the ability to occasionally track atmospheric water vapor anomalies before evolving into AR geometries, effectively tracking AR genesis further back than other studies. With the aid of subdaily satellite-derived rain data, we investigate the climatology, trends, and patterns of AR lifecycles from 1983–2016 and compare with other AR tracking studies. We find that AR frequency, genesis, and terminus locations are in generally good agreement with other AR tracking methodologies, though with key differences, and that AR frequencies in each hemisphere are determined by the number of AR hotspots. Furthermore, we uncover evidence that certain AR characteristics, such as frequency, areal extent, and duration, show evidence of increasing trends. Midlatitude precipitation uncovered by AR-CONNECT shows contributions up to 50% over land and 65% over the ocean. Trend analysis of AR precipitation shows an increase in precipitation associated with ARs propagated by the Southern Jet Stream and ARs that traverse over the Sahara Desert, among others, but is determined not to be a driver of changes in global precipitation.

Key Points:
- A region growing segmentation technique is used to track atmospheric rivers lifecycles by their higher-intensity cores
- The areal extent and duration of atmospheric river lifecycle are observed to be increasing over the study period of 1983–2016
- Precipitation from atmospheric rivers constitutes up to 50%/65% of the rainfall over the land/oceans and is shown to be increasing globally

Correspondence to:
E. J. Shearer,
eshearer@uci.edu

Citation:
Shearer, E. J., Nguyen, P., Sellars, S. L., Analui, B., Kawzenuk, B., Hsu, K., et al. (2021). Examination of global midlatitude atmospheric river lifecycles using an object-oriented methodology. *Journal of Geophysical Research: Atmospheres*, *125*, e2020JD033425. https://doi.org/10.1029/2020JD033425

Received 7 JUL 2020
Accepted 25 OCT 2020
Accepted article online 3 NOV 2020
Corrected 23 FEB 2021

This article was corrected on 23 FEB 2021. See the end of the full text for details.

1. Introduction

Atmospheric rivers (ARs) are long, transient atmospheric pathways of enhanced water vapor flux (Ralph & Dettinger, 2011; Zhu & Newell, 1998) typically associated with extratropical cyclones (ETCs) and frequently quantified by the integrated water vapor transport (IVT) variable (Rutz et al., 2014, 2019; Shields et al., 2018). ARs frequently produce heavy, impactful precipitation over where they are forced upward by orography (Ralph et al., 2004). While ARs and their impacts, which range from very beneficial to very detrimental, have traditionally been studied as a western U.S. phenomenon (Dettinger, 2011, 2013; Guan et al., 2010; Neiman et al., 2013; Ralph, Rutz, et al., 2019), it has become apparent that ARs affect many low-, middle-, and high-latitude regions of the world (Dezfuli, 2020; Gorodetskaya et al., 2014; Ramos et al., 2015; Thapa et al., 2018; Viale et al., 2018; Wille et al., 2019; Yang et al., 2018; and Esfandiari & Lashkari, 2020; to name a few).

The need to classify ARs globally has birthed a multitude of definitions and methodologies that attempt to unify the definition of ARs (Shields et al., 2018). From an impacts point of view, the differing geography and climate patterns across AR-affected regions make direct comparisons of AR intensity-impact relationships variable, creating difficulty in determining a one-size-fits-all threshold of IVT for global AR segmentation. Difficult as it may be, numerous studies have attempted to unify a definition of ARs using an absolute IVT definition (Rhoades et al., 2020; Rutz et al., 2014; Sellars et al., 2017) or relative definition, such as latitude-dependent (Lavers & Villarini, 2015) or pixel-based (Brands et al., 2017; Guan & Waliser, 2015).

ARs exist on synoptic time scales and travel distances of thousands of kilometers, requiring the development of tracking algorithms to study ARs from genesis to terminus, for example, AR lifecycles. One such methodology is the CONNected-objECT (CONNECT) algorithm (Sellars et al., 2013, 2015, 2017), which extracts hydroclimate features where they are contiguous over space and time. While not AR-specific, CONNECT run on IVT was invaluable for studies by the Atmospheric River Tracking Method Intercomparison Project (ARTMIP; Ralph, Wilson, et al., 2019; Rutz et al., 2019; Shields et al., 2018). Other AR lifecycle methodologies include Payne and Magnusdottir (2014), Zhou et al. (2018), and Guan and Waliser (2019), all of which are either based on a relative IVT threshold and/or are North American-centric.

In this study, the framework of CONNECT is altered to better extract ARs (AR-CONNECT). A seeded region growing segmentation methodology with static IVT thresholds is introduced to segment single AR lifecycles, offering an alternative to the methodologies introduced in Zhou et al. (2018) and Guan and Waliser (2019) to handle combination and separation in AR tracking. In this paper, we introduce the AR-CONNECT methodology and investigate the climatology, trends, and patterns of global midlatitude AR lifecycles and associated rainfall.

2. Data

2.1. IVT From MERRA-2

IVT data used in this data set were derived from the National Aeronautics and Space Administration's (NASA) Modern-Era Retrospective Analysis for Research and Applications-version 2 (MERRA-2) data (Gelaro et al., 2017), calculated from the following formula and used in the Tier 1 ARTMIP analysis—data ranges from January 1980–June 2017:

$$\mathbf{IVT} = -\frac{1}{g}\int_{p_{surf}}^{p_{200}} q\mathbf{V}\, dp$$

where p is pressure (hPa), p_{200} is the pressure at the 200 hPa level, p_{sfc} is pressure at the Earth's surface, q is specific humidity at height p, $\mathbf{V}$ is wind velocity (m/s), and g is gravitational acceleration. MERRA-2's high spatiotemporal resolution, proven accuracy, and emphasis on the hydrologic cycle (Rienecker et al., 2011) make it an invaluable tool for AR research. Moreover, MERRA-2's utility in producing the analysis done in Sellars et al. (2017) and proven skill for AR detection (Guan & Waliser, 2019; Jackson et al., 2016; Ralph, Wilson, et al., 2019) further cement its benefits for AR research.

2.2. Rainfall From PERSIANN-CDR

Precipitation Estimation from Remotely Sensed Information using Artificial Neural Networks-Climate Data Record (PERSIANN-CDR) is a 36 + year climate data record (1983 to present) of global precipitation that spans 60°N to 60°S with a spatiotemporal resolution of 0.25° and daily, derived from the PERSIANN algorithm (Hsu et al., 1997; Sorooshian et al., 2000) and bias-adjusted using the Global Precipitation Climatology Project (GPCP) monthly product. The quality of PERSIANN-CDR has been continuously evaluated by external researchers and continuously compares very favorably to the ground truth and other global satellite products (Guo et al., 2016; Miao et al., 2015; Nguyen, Ombadi, et al., 2018). PERSIANN-CDR's performance and quasi-global extent give the researchers in this study an opportunity to probe into the patterns and trends of global AR precipitation. PERSIANN-CDR is available from the CHRS Data Portal (Nguyen et al., 2019).

Given that MERRA-2 has a temporal resolution of 3 hr, we opted to use three-hourly PERSIANN-CDR data for rainfall mapping. Three-hourly PERSIANN-CDR should be considered experimental, as it's primarily used to produce publicly available PERSIANN-CDR data through daily averaging. As the time resolution is higher, there are issues with missing coverage. Therefore, for the rain trends plotted for section 4.3, only areas where there is coverage for at least 90% of the time steps are considered.

Analysis in this manuscript is done during the period where the MERRA-2 and PERSIANN-CDR data overlap to the last year of complete coverage: 1983–2016. Both variables are measured over simultaneous time windows, from 00z to 03z, 03z to 06z, etc. It should be noted that PERSIANN-CDR is an accumulative quantity, while IVT from MERRA-2 is a temporal average.

3. Materials and Methods

3.1. Object-Oriented Analysis

The methodology used to catalog AR lifecycle characteristics comes from the field of object-oriented analysis (Sellars et al., 2013). Object-oriented analysis is the study of the patterns in populations of objects from their attributes and statistics. In object-oriented analysis, "objects" are identifiable structures, events, anomalies, etc., that can be identified in a data set and represented by different statistics and attributes. For example, a hurricane identified from rainfall data can be represented by spatiotemporal features like volume and duration, target variable statistics like rainfall total, or climate indices like the state of the El Niño–Southern Oscillation (ENSO).

3.2. CONNECT

The CONNECT algorithm is an object-oriented, big data algorithm that uses three-dimensional (latitude, longitude, and time) pixels, also known as voxels, of a target variable (rainfall, temperature, etc.) to create objects constructed over where voxels are contiguous over space and time—by treating time as the z axis of a latitude-longitude space—and where the target variable is above a user-defined threshold, performed using a flood filling algorithm (Pavlidis, 1979). When studying synoptic scale, slow-moving phenomenon in high temporal resolution data, CONNECT performs well as a tracking algorithm, meaning objects segmented by CONNECT are the lifecycles of weather phenomena. CONNECT automatically stores each object into a table along with spatiotemporal, target variable, and climate oscillation characteristics calculated from the object.

The CONNECT methodology was developed for segmenting extreme rainfall events using the PERSIANN rainfall data set (Sellars et al., 2015). Subsequent work with CONNECT used the IVT variable to avoid segmenting one storm into multiple storms due to lulls in rainfall activity. However, using IVT to track objects with CONNECT (IVT-CONNECT; Sellars et al., 2017) proved difficult, as IVT values at AR levels exist in the atmosphere for prolonged periods in the tropics, which results in multiple events of enhanced IVT being combined into a single "conglomerate" object—not ideal for the extraction of singular AR lifecycles. Moreover, IVT-CONNECT extracts a multitude of tropical and non-AR activity, though it should be noted that IVT-CONNECT was not created as an AR-specific methodology.

3.3. AR-CONNECT

For this study, the CONNECT methodology was adapted to study the lifecycles of ARs. The following criteria were introduced to and adapted from CONNECT to create the AR-CONNECT framework (Figure 1; Shearer et al., 2020):

1. To overcome the challenges of conglomerate objects and henceforth isolate singular AR events, a seeded region growing segmentation technique (Adams & Bischof, 1994) was introduced.
2. To filter out tropical moisture features such as tropical cyclones and monsoons, objects with centroids inside of the tropical latitudes of 23.25°N to 23.25°S are filtered out. This means that an AR's genesis can be tropical, but the bulk of its volume should be primarily in the middle to upper latitudes.
3. IVT-CONNECT's minimum duration criteria of 24 hr is included in the AR-CONNECT methodology.
4. To quantify rainfall totals, PERSIANN-CDR (Ashouri et al., 2015) data are mapped to AR-CONNECT objects.

3.3.1. Region Growing Segmentation and IVT Thresholds

Region growing segmentation assumes that ARs have a core of enhanced IVT magnitude and uses this core to track and segment regions of enhanced IVT, similar to the methodology of Mundhenk et al. (2016). However, AR-CONNECT differentiates itself from other methodologies because it tracks where cores are contiguous over time and space before thresholding, meaning AR cores and bodies can be disconnected during one time step prior to later combination. At the same time, a region of enhanced IVT can be divided into several AR bodies equal to the number of cores within the boundary.

The thresholds utilized for the region growing technique are 700 and 300 kg m^{-1} s^{-1} for the AR core (seed) and the AR boundary (body), respectively. The threshold of 700 kg m^{-1} s^{-1} was adapted from the IVT-CONNECT700 catalog in the ARTMIP studies, which was found to capture the high-intensity cores of strong ARs and suffers very little from the conglomerate object problem thanks to its increased

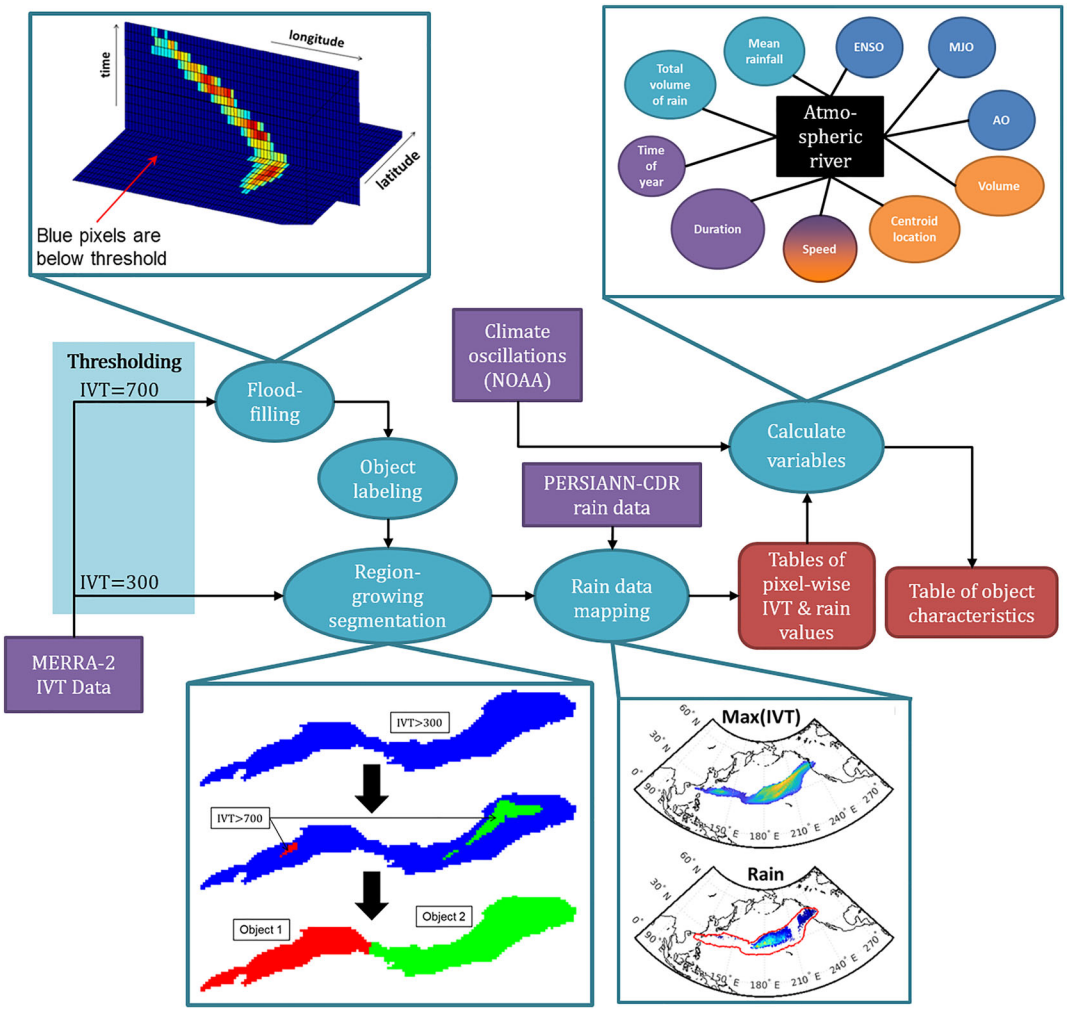

Figure 1. Schematic of the AR-CONNECT algorithm, with graphics for important processing steps. Purple indicates data inputs, blue demarcates processing steps, and red represents the output products of AR-CONNECT. Processing steps can be summarized thusly: IVT data from MERRA-2 is thresholded at two levels, IVT = 300 (AR body) or the IVT = 700 (AR core). Flood-filling involves finding all regions where IVT values at core levels are contiguous over time and space. This is the tracking portion of the AR-CONNECT methodology. Object-labeling involves giving each AR core object a unique identification number. Region growing segmentation is the process of growing the cores of an AR body, separating the AR body into individual AR lifecycles (labeled by the cores' object labels) at the IVT = 300 level. Rain data mapping is the process of mapping three-hourly PERSIANN-CDR to AR-CONNECT objects. Lastly, AR-CONNECT auto-calculates lifecycle characteristics like duration, speed, extent, rainfall volume, and many more.

threshold (Figure 2). The 300 kg m^{-1} s^{-1} threshold for the AR boundary is a rough average of the thresholds from Rutz et al. (2014) (250 kg m^{-1} s^{-1}), Ramos et al. (2018) (346–373 kg m^{-1} s^{-1}), and the range of thresholds calculated in Guan and Waliser (2015) (100–500 kg m^{-1} s^{-1}). The slightly elevated threshold of 300 kg m^{-1} s^{-1} means AR-CONNECT's utility is best in the midlatitudes, rather than at the poles.

3.3.2. Conglomerate Objects in AR-CONNECT

While the region growing technique used in AR-CONNECT does improve AR segmentation, it does not completely fix it, with a handful of objects being either too long in duration or too voluminous to be considered singular AR events. The limits of what constitutes a conglomerate object are either objects that are greater than 2 weeks in duration or $>10^9$ km^3 in time-integrated areal extent (area of AR per time step summed over each time step of the AR's lifecycle). The maximum duration of ARs are dominated by dynamics: ARs are a synoptic phenomenon that relies on the presence of ETCs that generally exist on time scales of days to weeks, with objects >2 weeks generally not occurring. Objects greater than this duration are

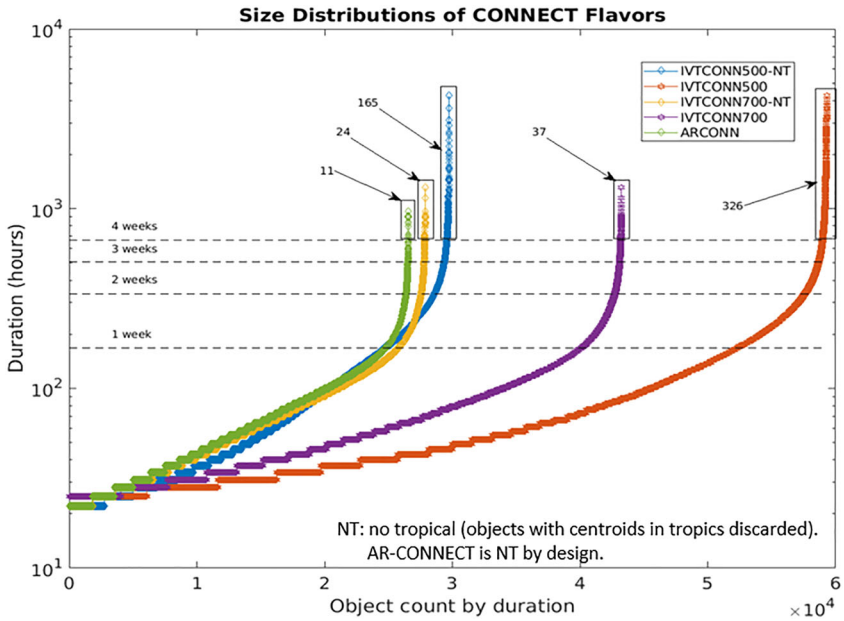

Figure 2. AR lifecycle durations depending on methodology. In the legend, the number indicates the IVT threshold used (300 kg m^{-1} s^{-1} for AR-CONNECT), and "NT" indicates the filtering of the parent algorithm's tropical objects (included in the AR-CONNECT framework). Numbers with arrows indicate the count of objects greater than 4 weeks in duration. Atmospheric dynamics implies that objects greater than a few weeks shouldn't be considered singular AR events and are considered conglomerate objects. This is reflected by the choice to use 2 weeks as the maximum duration for AR objects.

likely caused by the fusion of singular AR lifecycles rather than an anomalously long event. As for the area criteria, when sorting ARs from smallest to largest, at a value of 10^9 km^2, the curve of sorted AR areal extents begins to grow exponentially, indicating the undersegmentation of AR objects. In total, objects above either the conglomerate size or duration cut-off account for <1% of AR-CONNECT objects. While conglomerate objects will skew the averages of AR characteristics (Figures 5–7 and Table 1), they are important to quantify AR rainfall totals (Figure 8). Therefore, they are excluded from the former analyses but included in the latter. Furthermore, all AR-CONNECT objects are considered in the elongation calculation in section 4.1. Further developments in overcoming the conglomerate object problem are a continuing goal of research with AR-CONNECT.

Table 1
The Mean, Minimum, Maximum, and Standard Deviation of the Annual Frequency of Atmospheric Rivers (ARs) per Year and the Annual Averages of Three Important Characteristics of AR Lifecycles: Average Discrete Area, Duration, and Distance From the Equator

	Mean	Minimum	Maximum	Std. Dev.
Frequency of ARs	764	724	812	19.4
	312	286	339	10.6
	452	407	494	16.9
Average discrete area (km^2)	3.09×10^6	2.98×10^6	3.24×10^6	6.34×10^4
	2.92×10^6	2.77×10^6	3.18×10^6	8.59×10^4
	3.21×10^6	3.04×10^6	3.42×10^6	8.22×10^4
Duration (days)	3.12	2.99	3.28	7.07×10^{-2}
	3.25	3.07	3.41	8.96×10^{-2}
	3.04	2.88	3.22	8.75×10^{-2}
Distance from the equator (°)	39.8	39.0	40.6	0.389
	39.4	38.3	40.3	0.557
	40.0	39.4	41.0	0.471

Note. Values belonging to global ARs are in black, while values of ARs that inhabit the Northern and Southern Hemisphere are identified in red and blue, respectively.

4. Validation

4.1. AR-CONNECT as an AR Methodology

When considering AR tracking algorithms, one can classify different methodologies by the strictness of the requirements to classify a patch of enhanced IVT as an AR. Methodologies that have many and/or stricter requirements to consider an IVT pixel as part of an AR can be thought of as "restrictive" methodologies, while methodologies that have less strict or fewer requirements are considered "permissive." Another way to think about restrictiveness versus permissiveness is by the fractural coverage of Earth by ARs: On average, how much of the Earth's surface does an algorithm say is covered by ARs at any given moment? The more covered by ARs a methodology says the Earth is, the more permissive we may classify it. An example of a permissive algorithm is the methodology from Rutz et al. (2014), which only requires an IVT value >250 kg m^{-1} s^{-1} and a length >2,000 km, while IVT-CONNECT700 can be considered a restrictive algorithm owing to its high IVT requirement compounded by a 24-hr duration threshold. Though AR-CONNECT produces fewer objects than IVT-CONNECT700 (Figure 2), its objects contain on average 4 times more pixels than those from IVT-CONNECT700, making it a far more permissive methodology.

AR-CONNECT is developed to be a permissive algorithm, as its design was implemented, in part, to study global rainfall—a more restrictive design would cause significant underestimates to global rainfall totals. Moreover, AR-CONNECT aims to determine the genesis of ARs before growing to the geometric size or shape criteria commonly used in AR studies, that is, length >2,000 km and width <1,000 km (Wick et al., 2013). An example of this can be seen in the AR with genesis adjacent to South Africa shown in Figure 3. Because AR-CONNECT has no requirements for length, width, or shape, one may suspect that AR-CONNECT is a misnomer—not properly designed to track ARs, which are officially defined as "long, narrow" (Ralph, Rutz, et al., 2019), but rather a methodology to study regions of enhanced IVT. However, AR-CONNECT's methodology produces a catalog of ARs that follows common length criteria for ARs almost perfectly (Rutz et al., 2014; Wick et al., 2013). Of the entire catalog of AR-CONNECT objects, 99.99% are >2,000 km in length for at least one time step in its lifecycle. Moreover, in the Rutz methodology, a width requirement is not implemented, as it was observed that objects that were >2,000 km in length generally followed the shape requirement of being an AR. This same pattern was observed in the output of the AR-CONNECT algorithm, likely because both methodologies perform best for midlatitude studies. However, to prove this observation rigorously, during the time step where the object is at its greatest length, we analyze the ratio of the major axis to the minor axis of the ellipse with the same second moments as the object. We define suitable elongation as a ratio of the major axis to the minor axis of >2, equivalent to a commonly used ratio for AR geometry: >2,000 km in length and <1,000 km in width. Based on this metric, 89% of the AR-CONNECT objects have a suitable elongation to be defined as an AR. Moreover, we anticipate that the calculation of ellipses and axes does not consider curvature, which can cause the length of the minor axis to be far greater than the actual width. Therefore, we re-evaluate at a ratio of >1.5, enough to prove some degree of elongation and find that 97% of objects pass this lower metric. Lastly, we consider the shape index (AghaKouchak et al., 2011), a metric used to calculate the geometry of objects, at the object's greatest length. To be considered appropriately elongated, we set a minimum threshold of <0.75 based on Figure 7b from AghaKouchak et al. (2011), which shows an elongated object reminiscent of AR geometry. At this threshold, >99.99% of objects have a lower shape index. Furthermore, 97% of objects are lower than a more extreme shape index threshold of 0.60, and 88% are <0.50. With all these metrics combined, we conclude that objects segmented by AR-CONNECT show strong evidence of being both long and thin, circumventing the need to hard-code strict geometric criteria.

In short summation, AR-CONNECT finds a patch of IVT > 300 kg m^{-1} s^{-1}, and if it has a core of IVT > 700 kg m^{-1} s^{-1}, it is kept, regardless of geometry. By doing things this way, it is found that AR-CONNECT can track nonelongated IVT features that almost always evolve into AR geometries.

Lastly, as enhanced midlatitude IVT can be observed in ETCs (Mundhenk et al., 2016), some of the AR geneses extracted by AR-CONNECT are physically contiguous with ETCs (AR and ETC feature combined to form AR body), especially when the ETC doesn't have IVT values extreme enough to be affected by region growing segmentation. While this is a shortcoming of the methodology, the fact that 99.99% of objects are elongated to AR lengths means that the methodology does not regularly extract ETCs without an associated AR. Furthermore, it has been observed that ARs are associated with ETCs 82% of the time (Zhang et al., 2019),

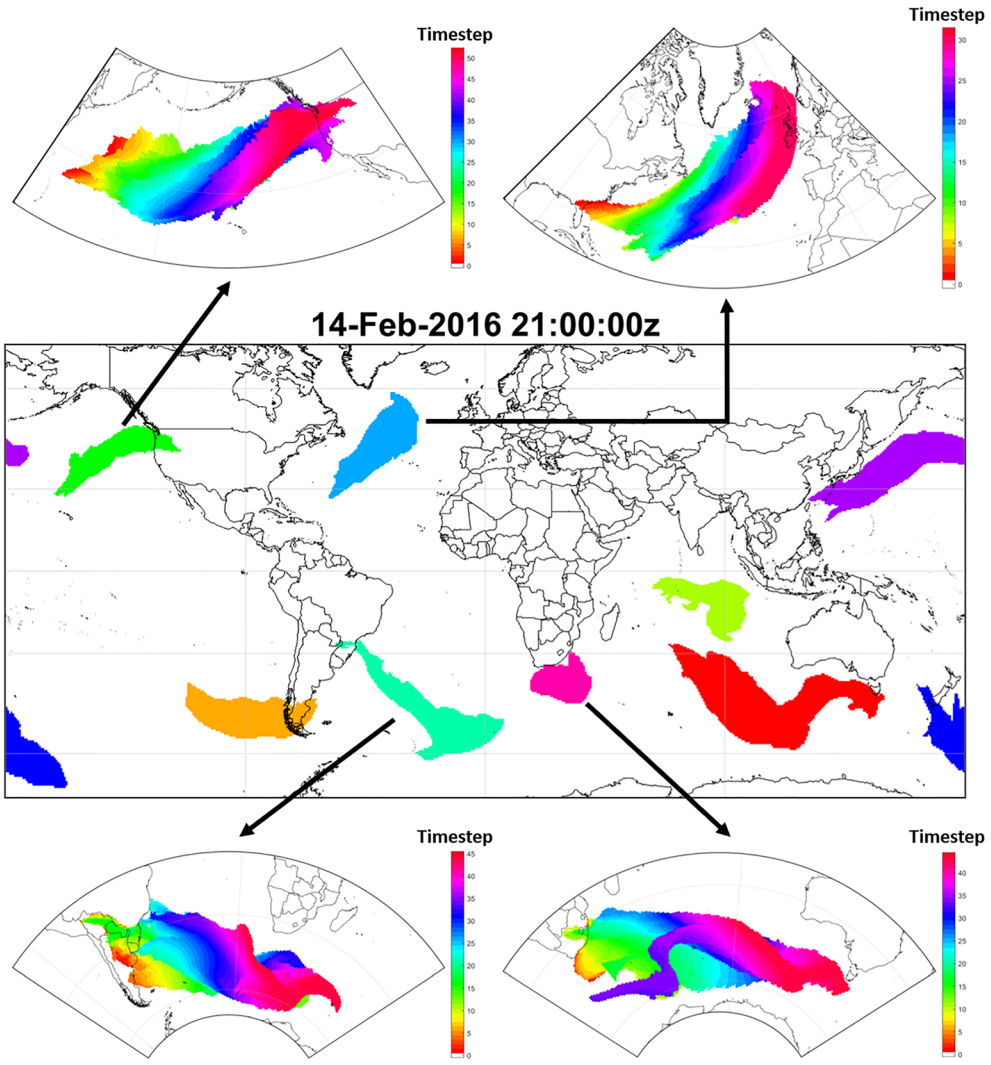

Figure 3. AR-CONNECT objects on 14 February 2016 at 21:00z. The lifecycles of four ARs, with pathways over the northern Pacific Ocean, the northern Atlantic Ocean, the southern Atlantic Ocean, and the Indian Ocean, are plotted to showcase their evolution and movement over their lifecycles. Of particular note is the AR over South Africa, which begins as a circular blob of IVT rather than an elongated shape more associated with ARs, subsequently evolves into longer and more elongated shapes over its lifecycle. This demonstrates one of the goals of AR-CONNECT: to identify ARs' origins before they resemble AR shapes.

especially during genesis, meaning that they are an important part of an AR's lifecycle and their extraction follows AR-CONNECT's goal of extracting AR genesis before reaching geometry that fulfills AR requirements.

4.2. Comparison to Other AR Tracking Methodologies

To showcase AR-CONNET's utility in the emerging field of AR tracking, we compare it to three pioneering methodologies: Payne and Magnusdottir (2014), Zhou et al. (2018), and Guan and Waliser (2019). The tracking methodology of Payne and Magnusdottir (2014) was developed to track large-scale ARs that made landfall on the West Coast of North America. The requirements for the algorithm, a discrete minimum areal size of 21,000 km^2 and a static IVT threshold of 350 kg m^{-1} s^{-1}, are too restrictive to capture the geneses of lifecycle ARs, making AR-CONNECT's ability to capture locations of AR genesis and its quasi-global extent a notable improvement over this methodology. Zhou et al. (2018) use a relative IVT threshold based on the 85th percentile of IVT per geographic location and season. Like Payne and Magnusdottir, Zhou's methodology is North American-centric. The AR tracking algorithm from Guan and Waliser (2019), named

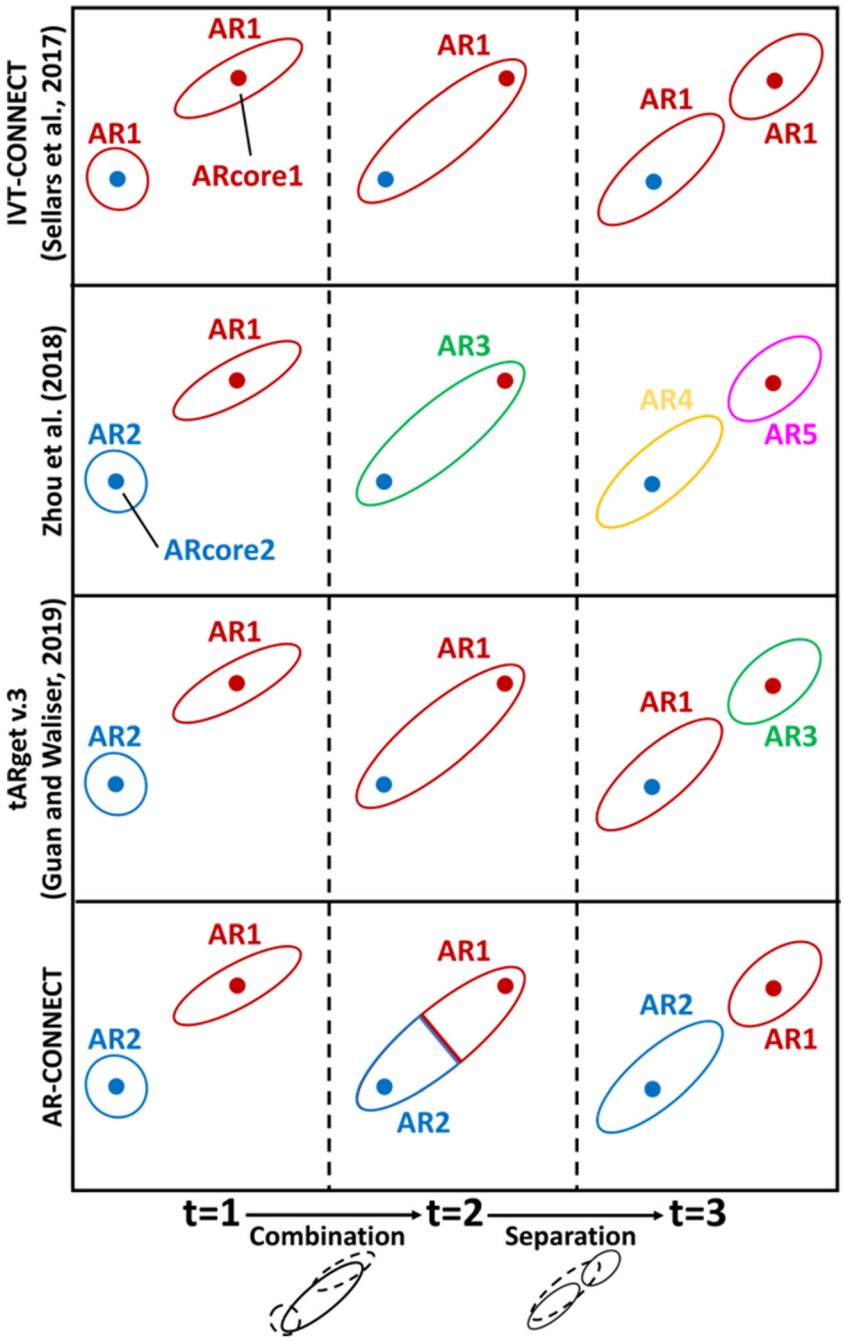

Figure 4. A comparison of how four different atmospheric river (AR) tracking methodologies handle a scenario where two AR bodies go through combination then separation over three time steps (t). The colored shape outlines, labeled as AR1–5 and color-coded, represents the body of the AR over each step of its lifecycle, while the filled color-coded dots, identified as ARcore1–2, represent the core of the AR (in this scenario, these cores are spatiotemporally contiguous per the requirements of AR-CONNECT.) Of each methodology, AR-CONNECT segments the lifecycle of ARs equal to the number of AR cores, while IVT-CONNECT combines all AR bodies into one lifecycle, Zhou et al. (2018) produce new ARs at every time step for a total of five, and tARget v.3, while showing skill in tracking ARs across the complicated scenarios inherent to AR tracking, does not track consistently with the AR core identities, falsely identifying the region surround ARcore2 as AR1.

tARget (v.3), utilizes a relative threshold >85th percentile like Zhou et al. (2018). Climatological-based methodologies continually demonstrate great utility, but their thresholds are not linked to impacts. Therefore, AR-CONNECT's usefulness exists in its threshold at levels where AR impacts are observable.

The biggest difference between AR-CONNECT, tARget, Zhou's methodology, and the IVT-CONNECT methodology from Sellars et al. (2017) is their treatment of separation, combination, and deformation, the background of which is explained in depth in Guan and Waliser (2019). Succinctly, IVT-CONNECT treats the combination of all IVT objects as a singular object, not treating the combination, division, or deformation of an AR as an AR genesis or terminus. Zhou and tARget both consider combination, division, and deformation in determining the genesis/terminus of ARs, but while Zhou considers each division or combination the start of a new AR, tARget aims to distinguish which AR is most similar from the previous step and assigns it to the next. For example, during a combination (two ARs combining into one; $2 \rightarrow 1$), tARget determines which AR from the previous step is most like the newly combined AR and assigns them the same identification number, while the other AR is considered terminating. Alternatively, during a separation (one AR dividing into two; $1 \rightarrow 2$), whichever AR is most like the AR from the previous step is considered a continuation, while the other is considered a genesis. AR-CONNECT, like IVT-CONNECT, elects to not consider combination, division, or deformation in AR tracking, preferring to segment based on AR cores. The advantage of this can be seen in Figure 4, where an idealized scenario of two ARs with distinct cores going through separation then combination is only successfully labeled according to their cores by the AR-CONNECT methodology.

4.3. Tracking AR Genesis

In section 4.1, it is claimed that AR-CONNECT can track ARs prior to growing into AR geometries. To concretely test this claim, every AR's genesis is examined by again calculating its shape index and length-to-width ratio. It is observed that in 22% (approximately one-in-five) of tracked ARs, the first time steps have not yet achieved AR geometries, which in this case we define as a shape index >0.60 or a length-to-width ratio of >2 (AR geometries will also be referred to as "elongation" hereafter). For these 22% of ARs that are tracked prior to elongation, it is calculated that they are tracked for an average of 12 hr before fulfilling AR geometry requirements.

One may question why the number of ARs that can be tracked prior to AR geometries is only one-in-five. This is the result of the combination and division of ARs, phenomena which are discussed in section 4.2. For example, if an elongated AR separates into two ARs because of the generation of a new AR core, the new AR may still be elongated during its first time step. Therefore, it would be impossible to track this AR before it attained AR geometries regardless of the methodology. Likewise, the enhanced core requirement of 700 kg m^{-1} s^{-1} is restrictive when considering genesis (though the extent of which is unknown), limiting the methodology from tracking more ARs geneses and/or tracking further back into AR genesis. Another point worth considering is that a new AR lifecycle created by separation appears to not be elongated when rather the object is a segmented piece of a segmented, elongated AR body. For example, examine Time Step 2 of AR-CONNECT in Figure 4. Both ARs combined make up an elongated AR body but individually are not elongated. If one of the AR cores had generated at this time step, it would be falsely considered to have been captured before elongation. Repeated instances of this scenario would inflate the total number of ARs captured before AR geometries, meaning the number of ARs captured before evolving into elongation is possibly lower than 22%. However, if this scenario was very common, we would expect to see radically different AR genesis hotspots than other studies. But when Figure 6b is observed, the pattern of AR genesis locations shows great similarity to that from Sellars et al. (2017), a methodology without seeded region growing segmentation, and therefore without separation-related genesis. Therefore, it can be assumed that this scenario is not responsible for a majority of the 22% of ARs tracked before elongation.

With these considerations, we attest that AR-CONNECT's ability to track AR genesis into earlier time steps is functional but far from perfect. It should be restated that the primary objective for the region growing methodology of this study was to fix the conglomerate object problem in IVT-CONNECT, which is the reason the more restrictive 700 kg m^{-1} s^{-1} threshold is used, the restrictiveness of which is balanced by the lack of geometric criteria. Without this criterion, it was hypothesized then observed that AR-CONNECT can track AR genesis into earlier time steps than other methodologies. Concretely, tracking AR genesis into earlier time steps is not a primary goal of the methodology but rather a side-effect of its design. Therefore, we argue that the results reported in this section should be considered a proof of concept for future work into AR genesis and AR tracking.

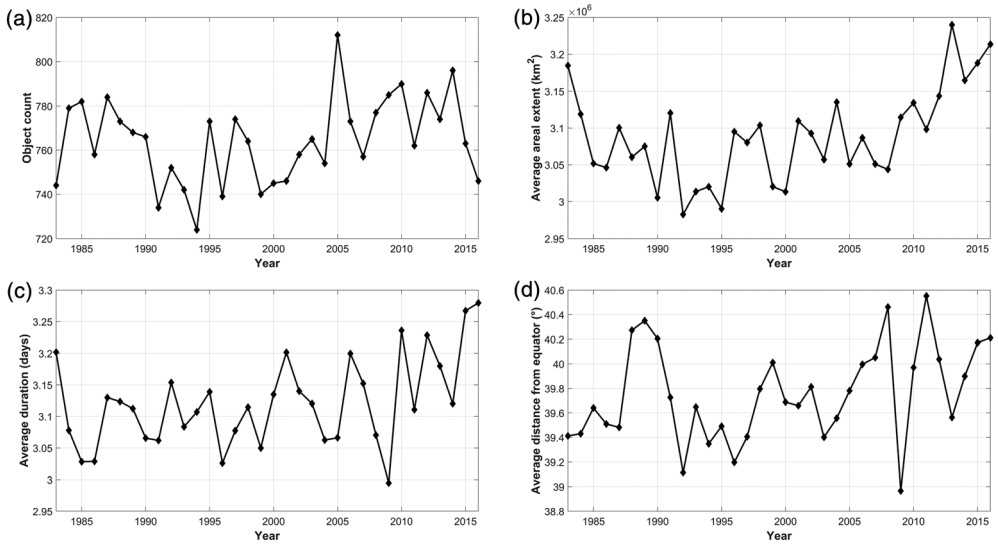

Figure 5. Annual AR characteristics over the past 34 years. (a) Frequency of global ARs per year. (b) Average discrete area (labeled as average areal extent). (c) Average AR duration per year. (d) Average AR's lifecycle weighted centroid distance from the equator.

Theoretically, to track ARs further into the beginning and end of AR lifecycles using the proposed methodology, future studies should consider using IVT climatology limits, as climatological-based AR tracking methodologies show greater ability to track AR inland penetration (Guan & Waliser, 2015). This theoretical methodology could be constructed in such a way where the 85th percentile of IVT is used to threshold the AR body and a significantly higher IVT climatology threshold is used to segment the AR core, likewise foregoing the need for hard-coded geometric criteria.

5. Results

5.1. AR-CONNECT Lifecycle Characteristics

The AR-CONNECT catalog currently consists of AR lifecycle objects described by a multitude of characteristics, including hydroclimate variables such as the average, maximum, median, sum, and standard deviation of the IVT field and the precipitation field; spatiotemporal variables such as each object's time-integrated areal extent ($TIA = \sum_{i=1}^{n} A_i$, where TIA is the total areal extent, n is the number of time steps of AR lifecycle, and A_i is the discrete area during time step i; this variable can be thought of as a pseudo-volume which considers the spatiotemporal extent of the object), speed, duration (number of time steps from genesis to terminus multiplied by 3-hr temporal resolution), lifecycle centroid (weighted centroid of AR over its lifecycle), genesis and terminus location, and genesis to terminus extent; and the states of 40 climate oscillation time series, including the Arctic Oscillation (AO), North American Oscillation (NAO), ENSO time series such as the Multivariate ENSO Index (MEI), and many more.

5.1.1. Climatology of AR-CONNECT Object Characteristics

We examine the total number of ARs per year and the annual averages of three characteristics useful to describe AR lifecycles: duration, average discrete area ($A_{ave} = \frac{TIA}{n}$; this variable is produced to remove the dependence between time-integrated areal extent and duration [correlation = 0.90]), and lifecycle centroid's distance from the equator. The annual time series of these variables is shown in Figure 3. We analyze each variable by taking the mean (found to be almost identical to the median for all variables), minimum, maximum, and standard deviation of each variable (Table 1) for the global, Northern Hemisphere, and Southern Hemisphere ARs.

When considering global ARs, we see an average of 764 ARs per year, each with an average discrete size of 3.09 million km^2, lasting for an average of 3.12 days with a center of mass at 39.8° from the equator. When looking at hemispheres, we see that there are a smaller number of Northern Hemisphere ARs, which are smaller in volume but greater in duration and closer to the equator than Southern Hemisphere ARs. The

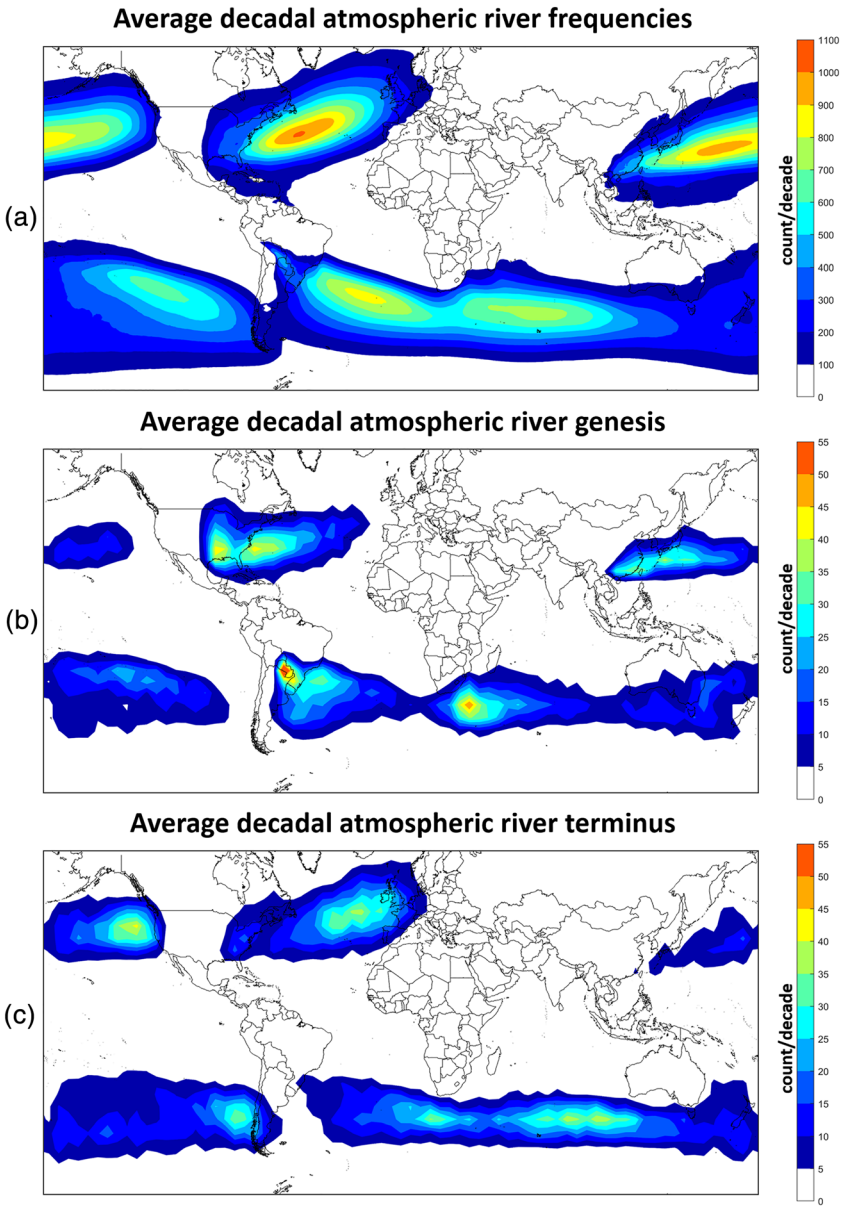

Figure 6. (a) The annual climatology of atmospheric river (AR) objects, and the decadal climatologies of (b) AR genesis and (c) AR terminus locations, resampled to a 5°-by-5° grid. Note the clear relationships between the three plots, demonstrating five notable hotspots: two in the Northern Hemisphere and three in the Southern Hemisphere, the latter of which are notably less distinguishable from each other.

ratio of AR counts per year between the Northern and Southern Hemispheres follow a ratio of approximately 2:3, which is equivalent to the number of AR hotspots observed in Figure 5c and found in Sellars et al. (2017) and Guan and Waliser (2019). Furthermore, we see that AR activity is slightly more stable in the Northern Hemisphere than in the Southern Hemisphere, where the standard deviation of annual AR counts is only 3.2% of the annual mean, compared to 3.7%. This is the only variable where the standard deviation is smaller in the Northern Hemisphere than the Southern Hemisphere, which in general have more consistency in the spatiotemporal characteristics studied. This is likely due to the disconnected nature of Northern Hemisphere AR tracks, creating distinct flavors of ARs between those over the Pacific and those over the Atlantic—notice the difference in track orientation, extent, and the more poleward extent of North Atlantic AR terminus locations—and is in stark contrast to the continuous AR track hotspots of the Southern Hemisphere (Figure 6a).

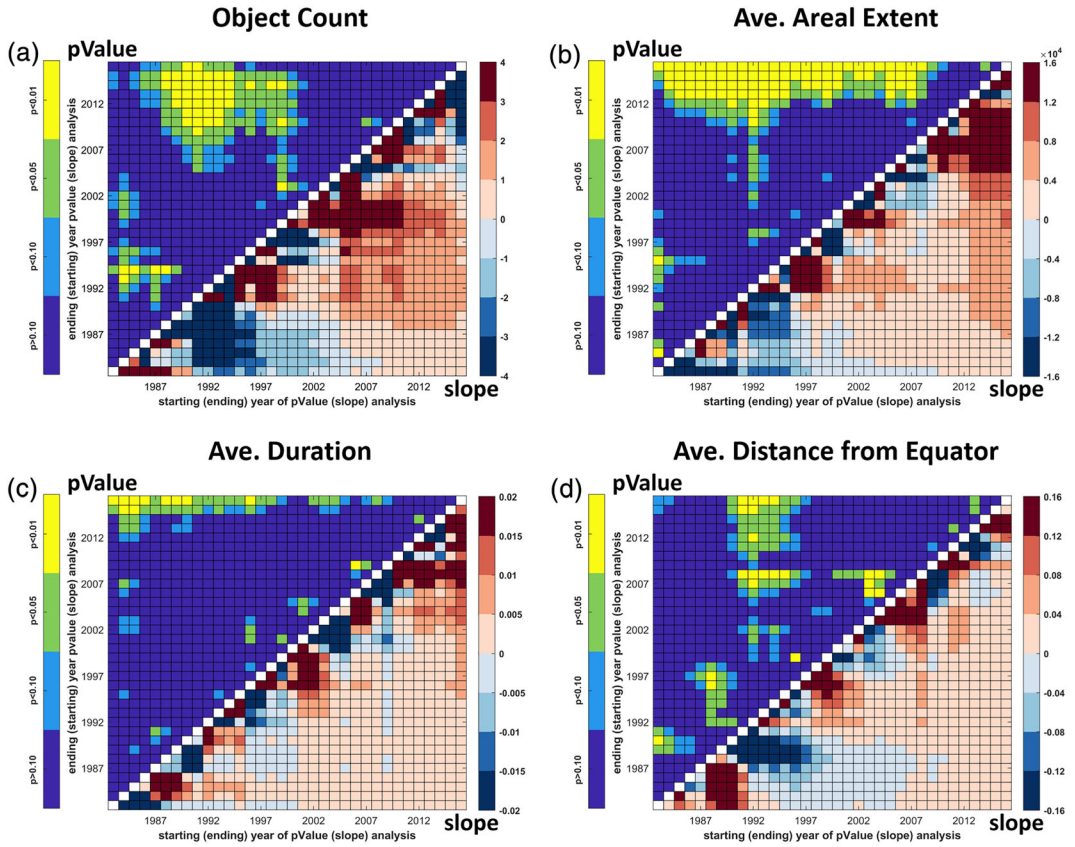

Figure 7. Trends in atmospheric river (AR) characteristics presented by slope and significance level (pValue) of the trend line (Figure 5). Points of trendline slope and pValue for identical time-periods are mirrored across the diagonal line of white grid-points. The greatest duration (1983–2016) subperiods can be observed in the top-left and bottom-right corners of the boxes for the pValue and slope, respectively. Each step left (right) of this point is a 1-year decrease in the ending year for the slope (pValue) time series, and each step up (down) of this point is a 1-year increase in the starting year for the slope (pValue) time series. For example, to investigate the trendline slope value from 1990–2010, we begin on the left-hand axis, identify the starting point of 1990 (two boxes below the 1992 tick), move horizontally across the diagonal white line, and stop where the bottom axis reads 2010 (two left of the 2012 tick). There, for plot 7a, we find a value of 1–2, indicating an average increase of one to two ARs per year over this period. Then, to identify the pValue, we begin from the bottom axis, identifying the starting point for 1990, move vertically past the line of white boxes, and end where the left axis reads 2010. Again, for plot 7a, we find a value of <0.05, indicating that our trendline slope of 1–2 is statistically significant at $\alpha = 0.05$. Each plot corresponds to the time series shown in Figure 5: (a) annual AR count, (b) average discrete area, (c) average duration, and (d) average distance from the equator.

Next, we examine the average decadal location of AR frequency, genesis, each averaged over a 5°-by-5° grid (Figures 6a–6c). We note AR hotspots over (1) the Northern Pacific, which consist of AR counts between 800 and 900 per decade, with genesis hotspots over southeast China and the northwest Pacific and terminus points over the Pacific coastline from California to the Aleutian Islands; (2) the northern Atlantic, with the greatest number of decadal ARs—greater than 1,000—with genesis over the eastern United States and northwestern Atlantic and terminus over northern and western Europe along with the adjacent parts of the Atlantic; and (3) Southern Hemisphere ARs, which exist continuously across the pathway of the Southern Jet Stream but show hotspots on both sides of South Africa and west of Chile. Notable genesis hotpots for these ARs include the region of the South American Low-Level Jet (Montini et al., 2019) and southeast of South Africa, with as many as 50 geneses, while there are notable terminus hotpots south of South Africa, in the southern Indian Ocean, and offshore of Chile.

These hotspots show good general agreement with the hotspots from Sellars et al. (2017), though the study includes signatures from objects in the tropical convergence zones. Furthermore, the genesis and terminus locations calculated here are in some agreement than those shown in Guan and Waliser (2019), which one

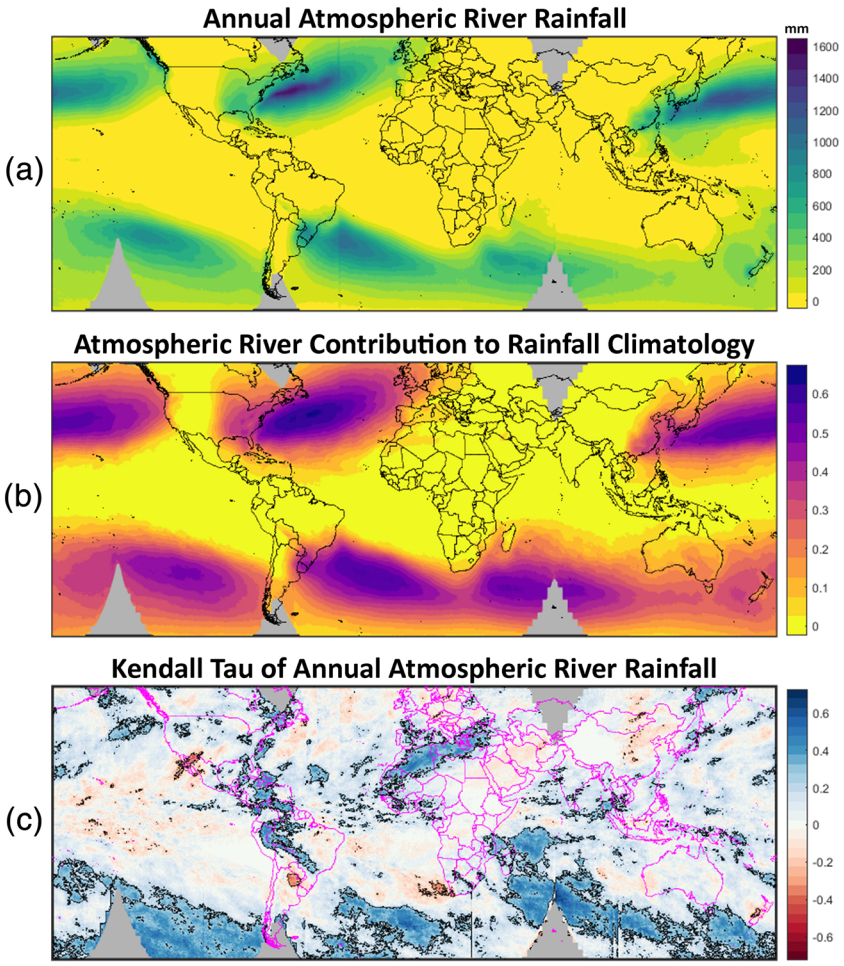

Figure 8. Global AR rainfall patterns and trends uncovered by AR-CONNECT and PERSIANN-CDR. Areas in gray are regions where data availability of three-hourly PERSIANN-CDR is <90% of time steps. (a) Average annual AR rainfall measured by PERSIANN-CDR. (b) Average annual AR precipitation (a) divided by annual rainfall climatology measured by PERSIANN-CDR. (c) Results of the Mann-Kendall test done at a significance level $\alpha = 0.05$. Values of Kendall's rank correlation coefficient (tau) are visualized by the red-white-blue color map, with regions of statistical significance indicated with a black outline.

would expect considering the difference in thresholding techniques and the lack of geometric criteria in AR-CONNECT. Again, it is worth noting that only 16% of ARs from AR-CONNECT are tracked during nonelongated genesis time steps, meaning we do not expect a radical difference in the heatmaps between AR-CONNECT genesis and other methodologies for this reason alone. One notable incongruency is the genesis locations calculated by AR-CONNECT show better agreement with the "spontaneous" genesis locations from Guan and Waliser's study than the overall frequency. This dissimilarity seems to stem from the existence of "separated-related" AR genesis in the upper latitudes, further poleward than where 300 kg m^{-1} s^{-1} IVT threshold is effective. When it comes to termination locations, the locations of Southern Hemisphere ARs recovered by tARget v.3 are again south of AR-CONNECT. This incongruency showcases the difference between the static IVT threshold used in AR-CONNECT to a relative one used in tARget. While AR-CONNECT captures the high-wind and moisture corridor of the Southern Jet Stream, tARget better identifies moisture plumes that exit the normative tracks and trend further poleward. We argue that both approaches have their merits: AR-CONNECT better captures lower-intensity ARs in the pathways of the Northern and Southern Jet Stream that tARget may not capture due to its thresholding requirements as high as ~500 kg m^{-1} s^{-1} in these regions, while tARget better captures ARs in the upper latitudes.

5.1.2. Trend Analysis of Global AR Lifecycle Characteristics

To understand how AR lifecycles have changed over our 34-year (1983–2016) catalog, we analyze the trends of the time series presented in Figure 5 by fitting a linear model. As the sensitivity of these trends during different periods of observation is high owing to the shorter-term domain of the catalog, we examine the trends across every multi-year period possible during the study duration, for a total of 561 trend analyses per variable (Figure 7). In this way, clusters of high values are clearly visible, and periods of enhancing or decreasing activity can be intuitively digested. Each trend analysis plot is divided into two halves: (1) the slope of the linearly fitted model and (bottom-right) (2) its statistical significance (probability value or "pValue," calculated from the model's *t*-statistic), shown in the top-left of each subfigure. Statistical significance is showcased at pValue intervals of [0.10, 0.05, 0.01].

The frequency (Figures 5a and 7a) of ARs per year shows a cluster of increasing AR values of slope between 2 and 4 ARs/year occurring between approximately 1985 and 2000 to approximately between 2005 and 2016. Another cluster of negatively trending values at a rate between 3 and 4 ARs/year exists between 1983 and 1989 to between 1991 and 1997. This suggests the possibility of a multidecadal oscillation in the number of AR appearances per year. When collectively considering the trend between 1984 to 2000 followed by the trend from 2000 to 2015, we see a near-perfect oscillation: −2 ARs/year in the falling limb followed by a 2 AR/year increase in the rising limb, both significant at a pValue = 0.05. Alternatively, one may consider longer-term trends, such as 1988–2015, which shows a robust trend at pValue<0.01 and an increase of ~1 AR/year. These results can be interpreted together: AR frequency shows evidence of following a multidecadal oscillating pattern forced slowly positive by a weak positive trend.

The trend of average discrete area (Figures 5b and 7b) shows a patch of statically significant and strongly increasing trends over longer (10-year +) time periods that end in the last 6–8 years of the record. Such a pattern indicates a strong positive signature in the IVT field, which is the result of anthropogenic heating creating a greater water vapor background climatology, translating into larger plumes of IVT above the 300 kg m^{-1} s^{-1} threshold (Espinoza et al., 2018; Wuebbles et al., 2017). For the duration time series (Figures 5c and 7c), only trends that end over the last 2 years of the study period show robustness when changing the beginning year. Even when considering the strongest trends, a total increase of only <0.20 days is observed, which is approximately equivalent to 1.5 time steps of the 3-hr temporal resolution of the MERRA-2 data set. Lastly, when considering the average distance to the equator (Figures 5d and 7d), a period of anomalously poleward centroids between 1990–1998 creates the signature of trends during most subperiods where the starting year is between 1990 and 1998. Moreover, when considering the longest-duration trend (1983–2016), there is a weak positive trend significant with a pValue <0.10, translating to an almost 1° migration of mean AR tracks poleward. In general, it seems that there is a relatively high amount of variance in this time series (Figure 5d), which makes a robust analysis of trends difficult.

Overall, the multisubperiod analysis presented in this study effectively makes diagnosing long-term trends from noise or decadal-scale oscillations more visually intuitive. Due to the shorter period of the analysis, there are still considerable questions regarding long-term trends, especially those influenced by anthropogenic climate change. Extending the time series into the past and future would give further insight into the trends of annual AR frequency, duration, and latitudinal location and is a promising direction for AR lifecycle research.

5.2. Rainfall Patterns

We plot the pattern of quasi-global (60°N to 60°S) annual AR rainfall climatology in Figure 8 and confirm the presence of sizable amounts of rainfall from landfalling ARs over regions frequently associated with AR activity such as the western United States; Chile; Europe, especially the British Isles; and Oceania. Furthermore, it is shown that regions associated with AR genesis, for example, central South America, the eastern United States, and eastern Asia, have a sizable portion of their rainfall climatologies from AR rainfall, with values up to 50%, though these totals (especially over the eastern United States) are likely exaggerated owing to the higher background moisture fields in these regions, which makes inadvertent capturing of convective systems in AR-CONNECT object boundaries likely.

In terms of validation, we examine that the precipitation fractions over the U.S. West Coast generally fall between 5% and 30% (Figure 7b), which is on the lower end to less than the 18–50% number given by

Dettinger (2011), Rutz et al. (2014), and Guan and Waliser (2015). This is expected, as the IVT threshold used in this analysis is greater than the 250 kg m^{-1} s^{-1} threshold typically used over the U.S. West Coast. Furthermore, these studies were done using daily precipitation products, while AR-CONNECT only accumulates precipitation totals during 3-hr increments of AR activity, a more conservative approach. Lastly, the numbers from Dettinger and Rutz are only calculated for the cool season.

Based on these results, we determine that the AR-CONNECT methodology demonstrates suitability for identifying regions of frequent AR activity and getting approximate AR rainfall totals and contributions to regional and global rainfall climatologies. For example, AR rainfall totals over Europe show contributions as great as 35% over coastal Ireland and contributions of at least 5% as far northeast as Russia and southeast as Iran. However, it is known that satellite measurements are less accurate than those from radar and rain gauges. Therefore, AR rainfall fractions presented in this study outside of well-studied regions like the west coast of North America need to be reinforced by other global and regional studies. We may start such analysis with Lavers and Villarini (2015), focused on North America and Europe, and Guan and Waliser (2015), which provides global analysis.

Lavers and Villarini's analysis over North America, which show generally good agreement in AR precipitation fraction over the western United States with AR-CONNECT, also has a similar pattern of eastern U.S. precipitation, though the fractions presented in Figure 7b tend to be about 10–15% greater, certainly due to Lavers and Villarini's higher IVT requirements over the region. Over Europe, the fractions calculated are in very good agreement with AR-CONNECT, especially over Iberia and Central Europe, though AR-CONNECT estimates a greater percentage of precipitation from ARs over the British Isles. Guan and Waliser's totals, despite being based on IVT climatology rather than a static IVT definition, show generally good agreement over Southern America, Europe, China, and Oceania, though there are very notable differences over regions where the background IVT is low, such as the Sahara Desert, the Middle East, and the Arctic. It is important to note that these studies also use daily precipitation accumulations to calculate rainfall totals, rather than at the subdaily scale like AR-CONNECT.

In terms of AR rainfall trends, trends in annual pixel rainfall totals are analyzed through the Mann-Kendall test at a significance level of $\alpha = 0.05$ and the Kendall rank correlation coefficient (Figure 8c). We choose to use the Kendall rank correlation, a trend analysis method closely related to the Mann-Kendall test, because it is not affected by missing data, which is an issue with the incomplete coverage of the satellite record back to 1983.

Kendall rank correlation (τ) is calculated thusly:

$$\tau = \frac{\sum_{i=1}^{n-1}\sum_{j=i+1}^{n}\mathrm{sgn}(x_j - x_i)}{n(n-1)/2}$$

where x is a single value from a vector of annual point rainfall values $\mathbf{x}$ and n is the population size of x. In essence, τ is the number of concordant pairs subtracted by the number of discordant pairs divided by the total number of pairwise comparisons, with [1–1] being the bounds of a perfectly increasing/decreasing time series.

Overall, when considering regions where there is satellite coverage ≥90% of the CDR data files, annual AR-related rainfall is increasing over 74% of the world's surface, with 17% showing a significant trend. Regions of enhanced rainfall include along the Southern Jet Stream, east of the Andes, and southern Europe to western Asia. The Sahara Desert also shows a significant positive trend. However, this region is one of the most problematic for remotely sensed quantitative precipitation estimation (Kelley, 2014) and should be considered with great scrutiny. Inversely, 23% of the world is seeing a decrease in AR rainfall, though <1% is statistically significant. Regions where AR rainfall is decreasing significantly include northern Mexico/the American Southwest, New Zealand, and northeastern Argentina, the most latter of which is the hottest spot of AR genesis (Figure 6b). The rainfall trend patterns presented in Figure 7c show some similarities to those in Nguyen, Thorstensen, et al. (2018), done to the same significance level and almost identical period (1983–2015). For example, both show evidence of decreasing precipitation over the equatorial Pacific and Southern Brazil/Uruguay, along with increasing trends over the equatorial Atlantic, the Eastern Pacific, and the Amazon Rainforest. However, when considering statistically significant trends,

there seems to be little agreement. For example, AR-CONNECT's strong signal over the Southern Jet Stream is almost nonexistent in Nguyen, Thorstensen, et al. (2018)'s study. It should be noted that increases in AR precipitation are likely in part a result of the nonstationarity of the IVT field per year, increasing the frequency that ARs exist over these regions and therefore increasing the frequency precipitation is linked to AR activity. However, increased atmospheric water vapor should also translate to greater AR precipitation totals (Espinoza et al., 2018). Therefore, the incongruency between the results of both studies suggests that changes in the global annual distribution of rainfall may not be driven by increasing AR activity.

6. Conclusions and Future Work

In this paper, the CONNECT algorithm is adapted to track the lifecycles of global midlatitude ARs and associated precipitation. This is done by tracking AR "cores," which is shown to be an effective way of extracting singular ARs lifecycles by reducing the existence of conglomerate objects. Furthermore, the new methodology allows AR-CONNECT to track AR geneses back to before they obtain AR geometries. Despite not having hard-coded geometric requirements to classify an IVT patch as an AR, analysis into the lengths and shape of AR-CONNECT objects show that in general, objects show suitable elongation during their lifecycles to be considered ARs.

Through the AR-CONNECT methodology, we investigate the climatology and trends of AR characteristics such as frequency, size, duration, and centroid location. Generally, the number of ARs lifecycles exists in a 2:3 ratio of Northern Hemisphere to Southern Hemisphere ARs, which is identical to the ratio of AR track hotspots in each hemisphere. Trend analysis indicates that there is a large statistically significant increase in the size of ARs, while there is evidence of an oscillating nature in annual AR numbers coupled with a small increasing trend, along with a minor increasing trend in duration, and a 1° poleward shift in AR tracks since 1983. In terms of validation, it is shown that the ARs follow the same tracks and have similar genesis/terminus locations as uncovered in Sellars et al. (2017) and Guan and Waliser (2019). Moreover, the AR rainfall contributions produced from AR-CONNECT and PERSIANN-CDR over the western United States fall within the lower limits of the results from Dettinger (2011), Rutz et al. (2014), Guan and Waliser (2015), and Lavers and Villarini (2015) and are in generally good agreement with the results from the non-western U.S. portion of the analysis from Lavers and Villarini (2015) and the midlatitude totals from Guan and Waliser (2015). The Mann-Kendall test located areas of significantly changing AR rainfall and found that 17% of the world between 60°N and 60°S is experiencing a statistically significant increase, though it is concluded that AR rainfall has likely not driven global annual precipitation pattern changes over the period.

The wealth of information collected by AR-CONNECT on AR lifecycles, especially the linkage of AR lifecycle characteristics with the states of climate oscillations, can prove to be valuable tools in investigating how these climate oscillations influence the characteristics of ARs. Future work will focus on such analysis with the hopes of improving our understanding of the link between them.

Data Availability Statement

Data are archived and available at the UC San Diego Library's Research Data Curation Program (https://doi.org/10.6075/J0D21W00), to whom we extend our sincerest thanks

Acknowledgments
This research was partially supported by the Ridge to Reef NSF Research Traineeship (#DGE-1735040) provided to the first author, Department of Energy (#DE-IA0000018), California Energy Commission (#300–15-005), the National Oceanic and Atmospheric Administration (#ST133017CQ0058) with Riverside Technology, Inc., and University of California (#4600010378 TO#15 Am 22). We also thank the anonymous reviewers for their comments and suggestions.

References

Adams, R., & Bischof, L. (1994). Seeded region growing. *IEEE Transactions on Pattern Analysis and Machine Intelligence*, *16*(6), 641–647. https://doi.org/10.1109/34.295913

AghaKouchak, A., Nasrollahi, N., Li, J., Imam, B., & Sorooshian, S. (2011). Geometrical characterization of precipitation patterns. *Journal of Hydrometeorology*, *12*(2), 274–285. https://doi.org/10.1175/2010JHM1298.1

Ashouri, H., Hsu, K. L., Sorooshian, S., Braithwaite, D. K., Knapp, K. R., Cecil, L. D., et al. (2015). PERSIANN-CDR: Daily precipitation climate data record from multisatellite observations for hydrological and climate studies. *Bulletin of the American Meteorological Society*, *96*(1), 69–83. https://doi.org/10.1175/BAMS-D-13-00068.1

Brands, S., Gutiérrez, J. M., & San-Martín, D. (2017). Twentieth-century atmospheric river activity along the west coasts of Europe and North America: Algorithm formulation, reanalysis uncertainty and links to atmospheric circulation patterns. *Climate Dynamics*, *48*(9–10), 2771–2795. https://doi.org/10.1007/s00382-016-3095-6

Dettinger, M. (2011). Climate change, atmospheric rivers, and floods in California—A multimodel analysis of storm frequency and magnitude changes. *Journal of the American Water Resources Association*, *47*(3), 514–523. https://doi.org/10.1111/j.1752-1688.2011.00546.x

Dettinger, M. D. (2013). Atmospheric rivers as drought busters on the U.S. West Coast. *Journal of Hydrometeorology*, *14*(6), 1721–1732. https://doi.org/10.1175/JHM-D-13-02.1

Dezfuli, A. (2020). Rare atmospheric river caused record floods across the Middle East. *Bulletin of the American Meteorological Society*, *101*(4), E394–E400. https://doi.org/10.1175/BAMS-D-19-0247.1

Esfandiari, N., & Lashkari, H. (2020). The effect of atmospheric rivers on cold-season heavy precipitation events in Iran. *Journal of Water and Climate Change*. https://doi.org/10.2166/wcc.2020.259

Espinoza, V., Waliser, D. E., Guan, B., Lavers, D. A., & Ralph, F. M. (2018). Global analysis of climate change projection effects on atmospheric rivers. *Geophysical Research Letters*, *45*, 4299–4308. https://doi.org/10.1029/2017GL076968

Gelaro, R., McCarty, W., Suárez, M. J., Todling, R., Molod, A., Takacs, L., et al. (2017). The Modern-Era Retrospective Analysis for Research and Applications, version 2 (MERRA-2). *Journal of Climate*, *30*(14), 5419–5454. https://doi.org/10.1175/JCLI-D-16-0758.1

Gorodetskaya, I. V., Tsukernik, M., Claes, K., Ralph, M. F., Neff, W. D., & Van Lipzig, N. P. M. (2014). The role of atmospheric rivers in anomalous snow accumulation in East Antarctica. *Geophysical Research Letters*, *41*, 6199–6206. https://doi.org/10.1002/2014GL060881

Guan, B., Molotch, N. P., Waliser, D. E., Fetzer, E. J., & Neiman, P. J. (2010). Extreme snowfall events linked to atmospheric rivers and surface air temperature via satellite measurements. *Geophysical Research Letters*, *37*, L20401. https://doi.org/10.1029/2010GL044696

Guan, B., & Waliser, D. E. (2015). Detection of atmospheric rivers: Evaluation and application of an algorithm for global studies. *Journal of Geophysical Research: Atmospheres*, *120*, 12,514–12,535. https://doi.org/10.1002/2015JD024257

Guan, B., & Waliser, D. E. (2019). Tracking atmospheric rivers globally: Spatial distributions and temporal evolution of life cycle characteristics. *Journal of Geophysical Research: Atmospheres*, *124*, 12,523–12,552. https://doi.org/10.1029/2019JD031205

Guo, H., Bao, A., Liu, T., Chen, S., & Ndayisaba, F. (2016). Evaluation of PERSIANN-CDR for meteorological drought monitoring over China. *Remote Sensing*, *8*(5). https://doi.org/10.3390/rs8050379

Hsu, K. L., Gao, X., Sorooshian, S., & Gupta, H. V. (1997). Precipitation estimation from remotely sensed information using artificial neural networks. *Journal of Applied Meteorology*, *36*(9), 1176–1190. https://doi.org/10.1175/1520-0450(1997)036<1176:PEFRSI>2.0.CO;2

Jackson, D. L., Hughes, M., & Wick, G. A. (2016). Evaluation of landfalling atmospheric rivers along the U.S. West Coast in reanalysis data sets. *Journal of Geophysical Research: Atmospheres*, *121*, 2705–2718. https://doi.org/10.1002/2015JD024412

Kelley, O. A. (2014). Where the least rainfall occurs in the Sahara Desert, the TRMM radar reveals a different pattern of rainfall each season. *Journal of Climate*, *27*(18), 6919–6939. https://doi.org/10.1175/JCLI-D-14-00145.1

Lavers, D. A., & Villarini, G. (2015). The contribution of atmospheric rivers to precipitation in Europe and the United States. *Journal of Hydrology*, *522*, 382–390. https://doi.org/10.1016/j.jhydrol.2014.12.010

Miao, C., Ashouri, H., Hsu, K. L., Sorooshian, S., & Duan, Q. (2015). Evaluation of the PERSIANN-CDR daily rainfall estimates in capturing the behavior of extreme precipitation events over China. *Journal of Hydrometeorology*, *16*(3), 1387–1396. https://doi.org/10.1175/JHM-D-14-0174.1

Montini, T. L., Jones, C., & Carvalho, L. M. V. (2019). The South American low-level jet: A new climatology, variability, and changes. *Journal of Geophysical Research: Atmospheres*, *124*, 1200–1218. https://doi.org/10.1029/2018JD029634

Mundhenk, B. D., Barnes, E. A., & Maloney, E. D. (2016). All-season climatology and variability of atmospheric river frequencies over the North Pacific. *Journal of Climate*, *29*(13), 4885–4903. https://doi.org/10.1175/JCLI-D-15-0655.1

Neiman, P. J., Ralph, M. F., Moore, B. J., Hughes, M., Mahoney, K. M., Cordeira, J. M., & Dettinger, M. D. (2013). The landfall and inland penetration of a flood-producing atmospheric river in Arizona. Part I: Observed synoptic-scale, orographic, and hydrometeorological characteristics. *Journal of Hydrometeorology*, *14*(2), 460–484. https://doi.org/10.1175/JHM-D-12-0101.1

Nguyen, P., Ombadi, M., Sorooshian, S., Hsu, K., AghaKouchak, A., Braithwaite, D., et al. (2018). The PERSIANN family of global satellite precipitation data: A review and evaluation of products. *Hydrology and Earth System Sciences*, *22*(11), 5801–5816. https://doi.org/10.5194/hess-22-5801-2018

Nguyen, P., Shearer, E. J., Tran, H., Ombadi, M., Hayatbini, N., Palacios, T., et al. (2019). The CHRS data portal, an easily accessible public repository for PERSIANN global satellite precipitation data. *Scientific Data*, *6*(1), 1–10. https://doi.org/10.1038/sdata.2018.296

Nguyen, P., Thorstensen, A., Sorooshian, S., Hsu, K., Aghakouchak, A., Ashouri, H., et al. (2018). Global precipitation trends across spatial scales using satellite observations. *Bulletin of American Meteorological Society*, *99*(4), 689–697. https://doi.org/10.1175/BAMS-D-17-0065.1

Pavlidis, T. (1979). Filling algorithms for raster graphics. *Computer Graphics and Image Processing*, *10*(2), 126–141. https://doi.org/10.1016/0146-664X(79)90046-7

Payne, A. E., & Magnusdottir, G. (2014). Dynamics of landfalling atmospheric rivers over the North Pacific in 30 years of MERRA reanalysis. *Journal of Climate*, *27*(18), 7133–7150. https://doi.org/10.1175/JCLI-D-14-00034.1

Ralph, F. M., & Dettinger, M. D. (2011). Storms, floods, and the science of atmospheric rivers. *Eos*, *92*(32), 265–266. https://doi.org/10.1029/2011EO320001

Ralph, F. M., Neiman, P. J., & Wick, G. A. (2004). Satellite and CALJET aircraft observations of atmospheric rivers over the Eastern North Pacific Ocean during the winter of 1997/98. *Monthly Weather Review*, *132*(7), 1721–1745. https://doi.org/10.1175/1520-0493(2004)132<1721:SACAOO>2.0.CO;2

Ralph, F. M., Rutz, J. J., Cordeira, J. M., Dettinger, M., Anderson, M., Reynolds, D., et al. (2019). A scale to characterize the strength and impacts of atmospheric rivers. *Bulletin of the American Meteorological Society*, *100*(2), 269–289. https://doi.org/10.1175/BAMS-D-18-0023.1

Ralph, F. M., Wilson, A. M., Shulgina, T., Kawzenuk, B., Sellars, S., Rutz, J. J., et al. (2019). ARTMIP-early start comparison of atmospheric river detection tools: How many atmospheric rivers hit northern California's Russian River watershed? *Climate Dynamics*, *52*(7–8), 4973–4994. https://doi.org/10.1007/s00382-018-4427-5

Ramos, A. M., Martins, M. J., Tomé, R., & Trigo, R. M. (2018). Extreme precipitation events in summer in the Iberian Peninsula and its relationship with atmospheric rivers. *Frontiers in Earth Science*, *6*. https://doi.org/10.3389/feart.2018.00110

Ramos, A. M., Trigo, R. M., Liberato, M. L. R., & Tomé, R. (2015). Daily precipitation extreme events in the Iberian Peninsula and its association with atmospheric rivers. *Journal of Hydrometeorology*, *16*(2), 579–597. https://doi.org/10.1175/JHM-D-14-0103.1

Rhoades, A. M., Jones, A. D., O'Brien, T. A., O'Brien, J. P., Ullrich, P. A., & Zarzycki, C. M. (2020). Influences of North Pacific Ocean domain extent on the western US winter hydroclimatology in variable resolution CESM. *Journal of Geophysical Research: Atmospheres*, *125*, e2019JD031977. https://doi.org/10.1029/2019JD031977

Rienecker, M. M., Suarez, M. J., Gelaro, R., Todling, R., Bacmeister, J., Liu, E., et al. (2011). MERRA: NASA's Modern-Era Retrospective Analysis for Research and Applications. *Journal of Climate*, *24*(14), 3624–3648. https://doi.org/10.1175/JCLI-D-11-00015.1

Rutz, J. J., James Steenburgh, W., & Martin Ralph, F. (2014). Climatological characteristics of atmospheric rivers and their inland penetration over the western United States. *Monthly Weather Review*, *142*(2), 905–921. https://doi.org/10.1175/MWR-D-13-00168.1

Rutz, J. J., Shields, C. A., Lora, J. M., Payne, A. E., Guan, B., Ullrich, P., et al. (2019). The Atmospheric River Tracking Method Intercomparison Project (ARTMIP): Quantifying uncertainties in atmospheric river climatology. *Journal of Geophysical Research: Atmospheres*, *124*, 13,777–13,802. https://doi.org/10.1029/2019JD030936

Sellars, S., Nguyen, P., Chu, W., Gao, X., Hsu, K. L., & Sorooshian, S. (2013). Computational earth science: Big data transformed into insight. *Eos (United States)*, *94*(32), 277–278. https://doi.org/10.1002/2013EO320001

Sellars, S. L., Gao, X., & Sorooshian, S. (2015). An object-oriented approach to investigate impacts of climate oscillations on precipitation: A western United States case study. *Journal of Hydrometeorology*, *16*(2), 830–842. https://doi.org/10.1175/JHM-D-14-0101.1

Sellars, S. L., Kawzenuk, B., Nguyen, P., Ralph, F. M., & Sorooshian, S. (2017). Genesis, pathways, and terminations of intense global water vapor transport in association with large-scale climate patterns. *Geophysical Research Letters*, *44*, 12,465–12,475. https://doi.org/10.1002/2017GL075495

Shearer, E. J., Nguyen, P., Sellars, S. L., Analui, B., Kawzenuk, B., Hsu, K. L., & Sorooshian, S. (2020). The Atmospheric River-CONNected objeECT (AR-CONNECT) algorithm applied to the National Aeronautics and Space Administration (NASA) Modern-Era Retrospective Analysis for Research and Applications, Version 2 (MERRA V2)—1983 to 2016. UC San Diego Library Digital Collections. https://doi.org/10.6075/J0D21W00

Shields, C. A., Rutz, J. J., Leung, L. Y., Martin Ralph, F., Wehner, M., Kawzenuk, B., et al. (2018). Atmospheric River Tracking Method Intercomparison Project (ARTMIP): Project goals and experimental design. *Geoscientific Model Development*, *11*(6), 2455–2474. https://doi.org/10.5194/gmd-11-2455-2018

Sorooshian, S., Hsu, K. L., Gao, X., Gupta, H. V., Imam, B., & Braithwaite, D. (2000). Evaluation of PERSIANN system satellite-based estimates of tropical rainfall. *Bulletin of the American Meteorological Society*, *81*(9), 2035–2046. https://doi.org/10.1175/1520-0477(2000)081<2035:EOPSSE>2.3.CO;2

Thapa, K., Endreny, T. A., & Ferguson, C. R. (2018). Atmospheric rivers carry nonmonsoon extreme precipitation into Nepal. *Journal of Geophysical Research: Atmospheres*, *123*, 5901–5912. https://doi.org/10.1029/2017JD027626

Viale, M., Valenzuela, R., Garreaud, R. D., & Ralph, F. M. (2018). Impacts of atmospheric rivers on precipitation in Southern South America. *Journal of Hydrometeorology*, *19*(10), 1671–1687. https://doi.org/10.1175/JHM-D-18-0006.1

Wick, G. A., Neiman, P. J., Ralph, F. M., & Hamill, T. M. (2013). Evaluation of forecasts of the water vapor signature of atmospheric rivers in operational numerical weather prediction models. *Weather and Forecasting*, *28*(6), 1337–1352. https://doi.org/10.1175/WAF-D-13-00025.1

Wille, J. D., Favier, V., Dufour, A., Gorodetskaya, I. V., Turner, J., Agosta, C., & Codron, F. (2019). West Antarctic surface melt triggered by atmospheric rivers. *Nature Geoscience*, *12*(11), 911–916. https://doi.org/10.1038/s41561-019-0460-1

Wuebbles, D. J., Easterling, D. R., Hayhoe, K., Knutson, T., Kopp, R. E., Kossin, J. P., et al. (2017). Our globally changing climate. In D. J. Wuebbles, (Eds.), *Climate Science Special Report: Fourth National Climate Assessment, Volume I* (pp. 35–72). Washington, DC: U.S. Global Change Research Program. https://doi.org/10.7930/J08S4N35

Yang, Y., Zhao, T., Ni, G., & Sun, T. (2018). Atmospheric rivers over the Bay of Bengal lead to northern Indian extreme rainfall. *International Journal of Climatology*, *38*(2), 1010–1021. https://doi.org/10.1002/joc.5229

Zhang, Z., Ralph, F. M., & Zheng, M. (2019). The relationship between extratropical cyclone strength and atmospheric river intensity and position. *Geophysical Research Letters*, *46*, 1814–1823. https://doi.org/10.1029/2018GL079071

Zhou, Y., Kim, H., & Guan, B. (2018). Life cycle of atmospheric rivers: Identification and climatological characteristics. *Journal of Geophysical Research: Atmospheres*, *123*, 12,715–12,725. https://doi.org/10.1029/2018JD029180

Zhu, Y., & Newell, R. E. (1998). A proposed algorithm for moisture fluxes from atmospheric rivers. *Monthly Weather Review*, *126*(3), 725–735. https://doi.org/10.1175/1520-0493(1998)126<0725:APAFMF>2.0.CO;2

Erratum

In the originally published version of this article, Figure 4 erroneously identified one study as "Zhang et al." instead of "Zhou et al." The figure also did not identify the atmospheric river cores explicitly mentioned in the caption. Figure 4 has since been corrected, and this version may be considered the authoritative version of record.